Detection of heartwood rot in Norway spruce trees with lidar and multi-temporal satellite data

Michele Dalponte [a,1,*], Yady Tatiana Solano-Correa [b,1], Hans Ole Ørka [c], Terje Gobakken [c], Erik Næsset [c]

[a] *Research and Innovation Centre Fondazione Edmund Mach, via E. Mach, 38010 San Michele all'Adige (TN), Italy*
[b] *University of Cauca, Calle 5 #4-70, 190003 Popayán, Cauca, Colombia*
[c] *Faculty of Environmental Sciences and Natural Resource Management, Norwegian University of Life Sciences, P.O. Box 5003, NO-1432 Ås, Norway*

ABSTRACT

Norway spruce pathogenic fungi causing root, butt and stem rot represent a substantial problem for the forest sector in many countries. Early detection of rot presence is important for efficient management of the forest resources but due to its nature, which does not generate evident exterior signs, it is very difficult to detect without invasive measurements. Remote sensing has been widely used to monitor forest health status in relation to many pathogens and infestations. In particular, multi-temporal remotely sensed data have shown to be useful in detecting degenerative diseases. In this study, we explored the possibility of using multi-temporal and multi-spectral satellite data to detect rot presence in Norway spruce trees in Norway. Images with four bands were acquired by the Dove satellite constellation with a spatial resolution of 3 m, ranging over three years from June 2017 to September 2019. Field data were collected in 2019–2020 by a harvester during the logging: 16163 trees were recorded, classified in terms of species and presence of rot at the stump and automatically geo-located. The analysis was carried out at individual tree crown (ITC) level, and ITCs were delineated using lidar data. ITCs were classified as healthy, infested and other species using a weighted Support Vector Machine. The results showed an underestimation of the rot presence (balanced accuracy of 56.3%, producer's accuracies of 64.3 and 48.4% and user's accuracies of 81.0% and 32.7% respectively for healthy and rot ITCs). The method can be used to provide a tentative map of the rot presence to guide more detailed assessments in field and harvesting activities.

1. Introduction

World forests are affected by several and different pathogens and insect attacks. Most of them usually result in the deterioration or death of large amounts of trees, hence increasing tree mortality and economical losses (Wermelinger, 2004). Some of these attacks are due to insects, whereas others are due to fungi. In any of the two cases, it is usually difficult to detect the infection in time to react and stop its spread across the forest. One of the most serious forest pathogens around Europe are the ones caused by fungal decay, where the decomposition of organic material can be seen on living trees, and is also known as rot. Depending on the fungus present, different organic materials are affected (Solheim, 2010).

There is a wide spread of fungi that causes rot (of root, butt and stem) and around 80% of the rot in the trees is caused by *Heterobasidion* spp.

and *Armillara* spp. (Solheim, 2010). The two fungi differ concerning distribution and host tree, but the most common fungi affecting Norway spruce in particular are the *Heterobasidion* spp. (Huse et al., 1994), which are further divided into two subspecies, being: *H. parviporum* and *H. annosum*. A tree attacked by such fungi experiences a decay in the heartwood that becomes rot. The fungus makes the wood taken from the trees only usable as pulpwood or as an energy source, thus substantially reducing the tree's economic value. Further, infection caused by *H. annosum* also reduces the tree growth rate, thus leading to a lower carbon sequestration and wood production (Oliva et al., 2012). Young infected trees usually die within three years. In older trees, the rot is chronic and develops internally, thus taking longer time for the tree to die (Solheim, 2010; Stenlid and Wästerlund, 1986). The most critical characteristic for *H. annosum* is that it can remain contagious for about 50 years after a final felling, thus requiring a proper treatment of the

remaining stumps and roots to prevent infection of the next generation of trees (Solheim, 2010).

Information regarding rot occurrence is essential for proper forest management and reduction of economic losses. One of the biggest challenges for early detection is the fact that there are almost no external visual signs of rot (Vollbrecht and Agestam, 1995). In particular, some studies showed that there is a difference in the crown density and structure between infected and healthy trees (Pitkänen et al., 2021; Žemaitis and Žemaitė, 2018). This change in any case is extremely difficult to note by visual inspection. Thus, detection of the infestation usually requires coring trees, a costly procedure when applied on a large scale. In fact, existing methods to provide relevant information for such goals are currently inefficient. The methods are time-consuming and performed manually on individual trees (Axmon et al., 2004), while rot can affect large areas within the forest, thus reducing detection efficiency. Hence, with the methods currently available, inventory of large forest areas would require extensive resources to get a clear picture of rot prevalence/infection (Leckie et al., 2004).

An alternative that could help to map extensive areas is the use of remotely sensed data. In fact, other plant diseases and pathogens have been detected with the use of remote sensing. Some of the health issues that have been studied include bark beetle infestations (Meddens et al., 2013), nutrient levels (Peng et al., 2020) and water stress (Fensholt et al., 2010). Root, butt and stem rot caused by fungi is definitely much more complex to detect: the rot usually is not affecting the living tissues of the trees, but only its core and thus the tree could be under no stress. However, some studies show a minor impact of rot to tree exterior (Žemaitis and Žemaitė, 2018). Despite this, some studies have been carried out using remotely sensed data acquired from aerial or satellite platforms to detect rot (Allen et al., 2022; Kankaanhuhta et al., 2000; Ostovar et al., 2019; Räty et al., 2021). Kankaanhuhta et al. (2000) used an airborne imaging spectrometer in order to obtain images from three forest areas in Finland at 1.6 m spatial resolution with 30 spectral channels and at two different dates. The study allowed the detection of healthy and infected trees in the area obtaining a detection rate of healthy trees between 72% and 90% and of infected trees between 94% and 96%. In a similar direction, Ostovar et al. (2019) made use of unmanned aerial vehicles (UAV) in order to detect rot stumps and measure the diameter of the rot stumps right after harvesting of the trees. While this information is relevant in order to understand the location of infected trees, it cannot help in detecting rot trees prior to harvest. Räty et al. (2021) predicted the volume of trees affected by butt rot in a spruce forest in Norway, using harvester, remotely sensed and environmental data. They found that remotely sensed predictor variables obtained from airborne laser scanning data and Sentinel-2 imagery were more important than the environmental variables in predicting butt rot volume. Allen et al. (2022) explored the use of airborne hyperspectral data to predict rot presence in trees in Norway. Their experiments showed that it is possible to predict rot presence at individual tree crown (ITC) level with 64% overall classification accuracy for presence absence classification of rot, leaving a margin for improvement.

In order to have an individual tree level detection of rot trees, it is necessary to have very high spatial resolution data. Indeed, many studies dealing with individual tree analysis are based on airborne data. The main limitation of such data is that they require ad hoc acquisitions and the acquisition of multi-temporal data may be expensive. Moreover, they do not allow covering very large areas. A possible alternative to such limitations is the use of satellite data with high spatial and temporal resolution, say, between 1 m and 10 m and 1 to 7 days, respectively. Nevertheless, even fewer studies can be found in literature that have exploited such types of data for the detection of rot in forests. Navarro-Cerrillo et al. (2019) performed an analysis with WordView-2 data (spatial resolution finer than 1 m) and lidar data in order to classify defoliation levels in *Quercus ilex* L. affected by rot. They reached a defoliation classification accuracy ranging between 85.1% and 86.7% with a kappa accuracy of 0.48–0.73. This task is different, and somehow

easier, than the rot detection itself, given the visual signs of infection. However, apart from the mentioned study, we are unaware of other studies on detection of rot infection in forest trees. However, several studies can be found in the context of precision agriculture, where satellite data such Sentinel-2 or Landsat have been used to detect rot in cotton and avocado with an overall accuracy ranging from 54% to 90%, depending on method and health status, among others (Peng et al., 2020; Pérez-Bueno et al., 2019; Song et al., 2017; Wu et al., 2018). In this case, the type of fungi is not the same as the one affecting Norway spruce trees, yet, the implications are the same: it affects the root at first and then it moves to upper areas of the plant. The fact that avocado trees have similar or smaller sizes than Norway spruce trees, and that root rot infection has been successfully detected at Sentinel-2 or Landsat spatial resolutions, allow us to think that it would be possible to use multi-spectral satellite data in order to map rot in Norway spruce trees. Using multi-temporal information may compensate for the lack of fine spatial information. There are several studies that have shown that adding the temporal dimension to the data can help to better map and understand the behaviour of a plant, disease or other phenomena, even though working with limited spatial resolution (Bovolo et al., 2018; Dalponte et al., 2020; Solano-Correa et al., 2020).

In the specific case of rot in Norway spruce trees, there is a clear need of developing a method that allows exploiting both fine spatial and fine temporal resolutions in order to properly map the infected trees. A map of this kind, included in a forest inventory, can contribute to tactical and operational decisions. This could result in a better economic outcome for the forest owners if used to take measures that reduce the negative effects of rot. In this context, this paper presents a complete system for detecting rot in Norway spruce trees that exploits multi-temporal satellite data acquired by the Dove sensor (3 m spatial resolution) in four different spectral channels. The Dove constellation is selected instead of other free alternatives (i.e., Sentinel-2) due to its higher spatial (3 m vs 10 m) and temporal resolutions (daily vs 5–10 days), been more suitable for the analysis at tree level. The proposed approach takes advantage of lidar data in order to delineate the individual tree crowns and further performs both tree species classification and rot detection in Norway spruce trees by a weighted Support Vector Machine (SVM) and vegetation indexes (VIs) extracted from multi-temporal Dove multi-spectral data. To the best of our knowledge, this is the first time that such an analysis has been carried out.

2. Materials and methods

In Fig. 1 the adopted processing architecture is shown. The final goal is to obtain a rot presence map at ITC level, thus both tree species classification and rot detection steps are needed. In the following paragraphs all the data used and the adopted processing steps are described in detail.

2.1. Study area, field data and remotely sensed data

The study area is located in Etnedal municipality, south-eastern Norway, covering 4.2 km^2 (Fig. 2). The area has steep terrain, an altitude ranging from 450 to 710 m above sea level, and the forest cover is dominated by Norway spruce (*Picea abies* (L.) Karst.), with Scots pine (*Pinus sylvestris* L.) and few broadleaves species.

The field data were collected in 2019–20 by a harvester during the logging. In total, 16,163 trees were recorded and automatically geo-located (Noordermeer et al., 2021). For each logged tree, the harvester operator registered the tree species, the diameter of the stump and the rot status at stump (presence or no presence). Norway spruce represented the majority of the harvested trees (16,210 trees), followed by Scots pine (1832 trees), and broadleaves species (890 trees). The harvester operator did not categorize some trees (231) in species because they were heavily damaged or dead. Among the Norway spruce trees, 13,195 were classified as healthy, while 3015 were affected by rot.
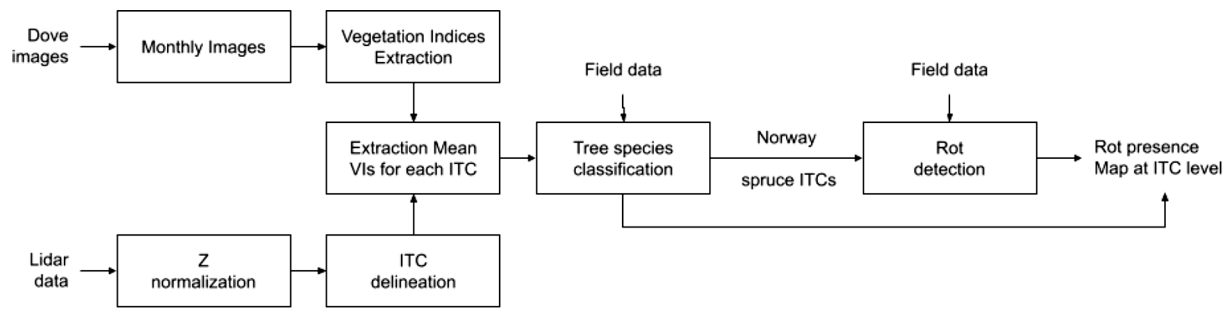
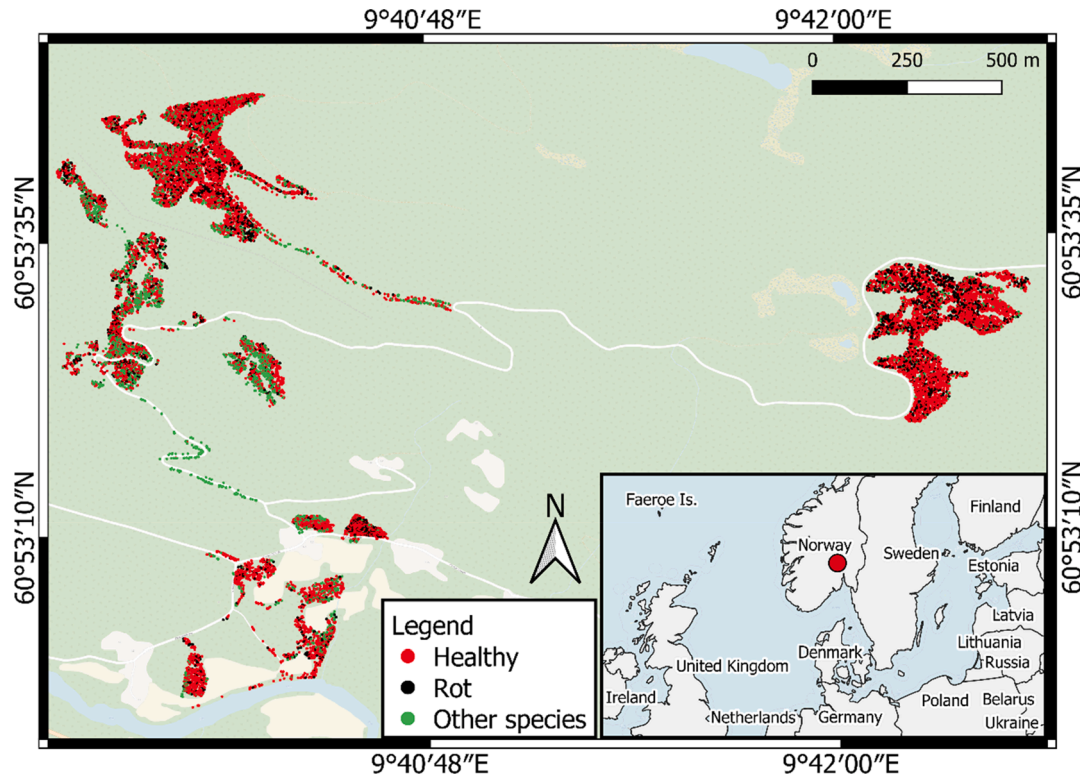**Fig. 1.** The adopted processing architecture.

Fig. 2. Location of the field trees (red, black and green dots in the large map), and location of the study area (red dot in the inset). (For interpretation of the references to colour in this figure legend, the reader is referred to the web version of this article.)

The species of the fungi causing the rot was not determined as no laboratory analysis was conducted.

Satellite multi-spectral images used in this study were acquired with the Dove constellation (also called PlanetScope). Dove is a constellation of >200 nano-satellites owned by the imaging company Planet Labs, Inc. (PlanetTeam, 2017), launched in 2017 and providing daily high resolution multi-spectral images at its full capacity, composed by four spectral bands at 3 m spatial resolution: blue (455–515 nm), green (500–590 nm), red (590–670 nm), and near-infrared (780–860 nm). Each Dove multi-spectral image covers an area of 24 × 8 km. Though Dove is a commercial satellite system, many of its products are free for research purposes and they can be downloaded from their website (https://www.planet.com). Concerning commercial use, Sozzi et al. (2018), in a study that compared pricing of different satellite constellations, reported a price of 0.012$/ha with a minimum order of 10,000 ha. All the available images in the study area for the months of May, June, July, August and September 2017, 2018 and 2019 were downloaded. Only the images without cloud cover or snow over the study area were kept. A further visual check regarding co-registration problems between images was performed in order to remove those that could introduce noise or

errors in the multi-temporal analysis. This procedure was carried out manually, but it could be easily automated. Moreover, in an operational scenario could be worth to consider to apply an algorithm for automatic image co-registration (i.e. (Dawn et al., 2010; Tondewad and Dale, 2020)) in order to improve the co-registration among images and increase the size of the dataset. The previous conditions lead us to work with a total of 53 images (Fig. 3, Table S1). The number of images in 2017 was small compared to 2018 and 2019, as the Dove constellation was not fully operational in 2017 and thus in May and September 2017 no suitable images were available.

Lidar data were collected on August 3rd, 2019 with the Leica ALS70-HP recording system mounted on a fixed-wing aircraft flying at 1150 m above ground level with a scan angle of 16°, a pulse repetition frequency of 495.2 kHz and a scan rate of 68.9 Hz, resulting in a point density of 17.6 pts/m². Up to four returns per pulse were recorded.

2.2. Remotely sensed data pre-processing

The lidar point cloud was normalized to height above ground by the vendor. Individual tree crowns were delineated on the normalized lidar
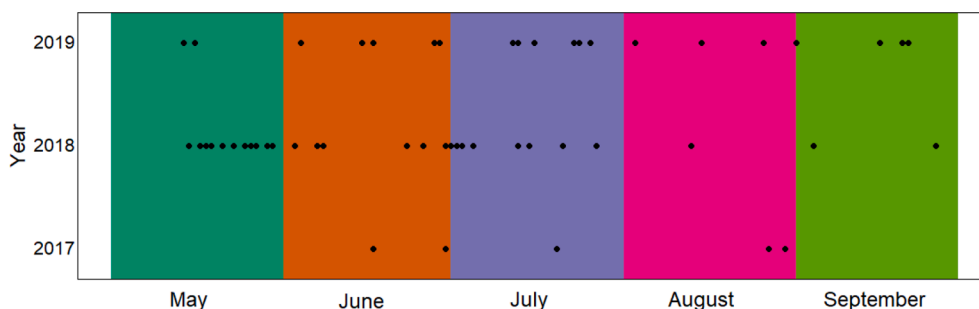
Fig. 3. Distribution of the Dove images over the months and years considered in this study.

point cloud using the algorithm of Dalponte and Coomes (2016) implemented in the function *itcLiDAR* of the R library *itcSegment*. This algorithm is based on an adaptive local maxima filter and a region growing method and it has been used successfully in many previous studies (Coomes et al., 2017; Dalponte et al., 2018; Dalponte and Coomes, 2016; Nguyen et al., 2019; Versace et al., 2019). In greater detail, the algorithm follows two main steps: (1) local maxima extraction: a circular moving window of variable size is applied to the CHM (previously smoothed with a 3x3 low pass filter) to find a set of potential treetops (local maxima). A pixel of the CHM is labelled as local maxima if its value is greater than all other values in the window while being greater than some minimum height above ground. The window size is adapted according to the height of the central pixel of the window, which is predetermined in a user-defined look up table; (2) crown region growing: the algorithm iteratively searches for possible neighbouring pixels to grow the crown of the tree around each local maxima. A pixel belongs to a specific region only if its vertical distance from the local maximum is less than a predefined percentage of the local maximum height, and less than a predefined maximum difference. The process repeats until no further pixel is added to any region. Once the region is fully grown, a 2D convex hull is applied, resulting in polygons that represent ITCs. The delineated ITCs were matched with the field-measured trees using a weighted Euclidean distance between the delineated ITCs and the field data coordinates (Zhao et al., 2018). In particular, the X and Y coordinates were used along with the height. For the delineated ITCs, the height used was the maximum height of the lidar points inside the ITC, while as field height we used the one estimated by the harvester. As this height is subject to some degree of error

the height was weighted less in the Euclidean distance calculation as suggested by (Zhao et al., 2018). In total, 8489 field trees were linked to a delineated ITC, out of which 7343 were identified as spruce trees according to the field recording.

Given that Dove images can be acquired by different satellites and at different times of the day, radiometric differences can appear within the images that can be understood as possible changes. In order to avoid such errors, and considering the slow evolution of the rot infection, the Dove images were aggregated into 13 groups corresponding to the months of i-iii) June, July, and August 2017 (3 months), iv-viii) May, June, July, August and September 2018 (5 months) and ix-xiii) May, June, July, August and September 2019 (5 months). Images of each group were averaged per band in order to obtain one composite multi-band image per month (13 images, one per month).

2.3. Feature extraction

From each of the 13 Dove monthly composite images a series of vegetation indices (VIs) were extracted (Table 1) using the function *spectralIndices* of the R package *RStoolbox* (Leutner et al., 2019). The VI chosen were the most common indices that could be extracted when having four available bands (RGB + NIR). We considered only normalized VIs as they are more suitable for multi-temporal analyses. For the same reason we did not use the individual bands in the classification.

Each ITC could cover more than one pixel of VI with different percentage of overlap, thus the weighted average of the pixels of VI images overlapping with each ITC was calculated in order to have one value for each VI, month of the year and ITC, thus reducing possible spectral

Table 1
Vegetation indices extracted from each Dove image.

Vegetation index	Equation	Reference
CTVI - Corrected Transformed Vegetation Index	$\dfrac{NDVI + 0.5}{\sqrt{\lvert NDVI + 0.5 \rvert}}$	(Perry and Lautenschlager, 1984)
GEMI - Global Environmental Monitoring Index	$\eta*(1 - 0.25*\eta) - \dfrac{red - 0.125}{1 - red}$ with $\eta = \dfrac{2*\left(NIR^2 - red^2\right) + 1.5*NIR + 0.5*Red}{NIR + red + 0.5}$	(Pinty and Verstraete, 1992)
GNDVI - Green Normalised Difference Vegetation Index	$\dfrac{NIR - green}{NIR + green}$	(Gitelson and Merzlyak, 1998)
MSAVI - Modified Soil Adjusted Vegetation Index	$NIR + 0.5 - \left(0.5*\sqrt{2*NIR + 1}\right)^2 - 8*(NIR - (2*red))$	(Qi et al., 1994)
MSAVI2 - Modified Soil Adjusted Vegetation Index 2	$\dfrac{2*NIR + 1 - \sqrt{(2*NIR + 1)^2 - 8*(NIR - red)}}{2}$	(Qi et al., 1994)
NDVI - Normalised Difference Vegetation Index	$\dfrac{NIR - red}{NIR + red}$	(Rouse, J.W et al., 1974)
NRVI - Normalised Ratio Vegetation Index	$\dfrac{\frac{red}{NIR} - 1}{\frac{red}{NIR} + 1}$	(Baret and Guyot, 1991)
SAVI - Soil Adjusted Vegetation Index	$\dfrac{(NIR - red)*1.5}{NIR + red + 0.5}$	(Huete, 1988)
TTVI - Thiam's Transformed Vegetation Index	$\sqrt{\left\lvert \dfrac{NIR - red}{NIR + red} + 0.5 \right\rvert}$	(Thiam, 1998)
TVI - Transformed Vegetation Index	$\sqrt{\dfrac{NIR - red}{NIR + red} + 0.5}$	(Bannari et al., 1995)

variation/noise inside the ITCs. The weighting was conducted by resampling all VI images to 0.5 m. Dove pixels were divided into 36 pixels of 0.5x0.5 m, all with the same value as the original pixel (at 3x3m spatial resolution). Furthermore, pixels within each ITC were averaged, and in this way a weight was assigned to the original pixels depending on the magnitude of its overlap with the ITC.

2.4. Classification method

The tree species classification and rot detection were done using a class-weighted Support Vector Machine (wSVM) (Nguyen et al., 2019). SVM is a well-known classifier used in many forestry and ecological studies (Chen et al., 2017; Dalponte et al., 2014; Durbha et al., 2007; Gavier-Pizarro et al., 2012; Su et al., 2015), and in the wSVM a weight is added inside the optimization problem of the SVM. We chose a class-weighted version as it is more suitable for imbalanced problems, such as cases where there is a predominant class (the class "healthy" in this study) and a rare class (the class "rot" in this study). A possible disadvantage of using such methods is that they usually increase the commission errors for the dominant class, but we considered this an acceptable trade-off to improve the rot detection.

Let us assume to have a set S containing labeled training sample units with their weights $\{(x_i, y_i, s_i)\}_{i=1}^{N}$, where x_i is the training sample unit i, y_i is the corresponding label from the pool of the classes $K = k_1, \cdots, k_{\Psi}$, and s_i is the corresponding weight. The SVM soft margin optimization problem could be formulated as:

$$\frac{1}{2}||w||_2^2 + C\sum_{i=1}^{N} s_i \xi_i$$

$$\text{subject to}: \begin{cases} y_i(\omega.\Phi(x_i) + b) \geq 1 - \xi_i \\ \xi_i \geq 0, i = 1, \cdots, N \end{cases} \quad (1)$$

where Φ is the mapping function that projects the sample units from the original variable space to a higher dimensional space and b is a constant term. C is a regularization (i.e., penalty) parameter. The penalty value C of mis-classification for each training sample unit has a different weighting effect that is driven by s_i. s_i is defined according to the following equation:

$$s_i = \frac{\max\limits_{k=1,..,\Psi}(N_k)}{N_i} \quad (2)$$

where N_k is the number of sample units that belong to the k-th class.

2.5. Experimental design

Experiments for both tree species classification and rot detection were carried out considering different sets of features, different time periods and different subsets of ITCs both utilizing uni-temporal and multi-temporal data (see Table 2). In particular, for ITC subsets we considered two different options: (1) all ITCs and (2) only the ones with area above 9 m². We used a threshold of 9 m² as it represents the original size of a Dove image pixel (3x3m). For the features, we considered 11 options: (1) all indices together, or (2)-(11) every individual index alone (e.g., CTVI, GEMI, GNDVI, MSAVI, MSAVI2, NDVI, NRVI, SAVI, TTVI, TVI). Regarding time periods, we considered 22 options: (1)-(13) uni-temporal time slots (June 2017, July 2017, August 2017, May 2018, June 2018, July 2018, August 2018, September 2018, May 2019, June 2019, July 2019, August 2019, September 2019), and (14)-(22) multi-temporal time periods (all, 2017, 2018, 2019, May, June, July, August, and September). A total of 484 combinations of ITC sizes (n = 2), features (n = 11) and time periods (n = 22) were analysed. For each combination, we performed a nested cross-validation: one to select the best parameters of the wSVM and one to provide the average accuracies for each combination of ITC subsets, features and time periods. The

Table 2
Summary of the analysed ITC subsets, vegetation indices (VIs), and time periods.

ITC subsets	VIs	Time periods	
		Uni-temporal	Multi-temporal
All	All	June 2017	All
Area > 9 m²	CTVI	July 2017	2017
	GEMI	August 2017	2018
	GNDVI	May 2018	2019
	MSAVI	June 2018	May
	MSAVI2	July 2018	June
	NDVI	August 2018	July
	NRVI	September 2018	August
	SAVI	May 2019	September
	TTVI	June 2019	
	TVI	July 2019	
		August 2019	
		September 2019	

kernel function used in the wSVM was a radial basis function (RBF) kernel and the parameters optimized by a 5-fold cross validation were C and sigma. Nine C values and 50 sigma values were evaluated generating 450 combinations. Regarding the external cross-validation, we considered a 5-fold cross-validation built on a 100x100 m spatial grid over the study area (Solano-Correa et al., 2019). All the ITCs inside one square of the grid were assigned to one fold. In this way, we reduced the correlation among ITCs of training and validation without losing the representativeness of each fold in the study area.

As the main scope of this paper is the rot detection, we will first present the detailed results for this task, then we will show the results for the tree species classification, and lastly we will show the map of rot infection in Norway spruce trees that is the combination of the two classifications. The classification map at ITCs level (for both spruce and rot) was constructed using the model for all ITCs. Firstly, we created the map of "Norway spruce" vs. "Other species" and then we classified the Norway spruce ITCs in "Rot" and "No rot".

The classification results are presented in terms of overall accuracy (OA), producer's accuracy (PA), user's accuracy (UAs) and balanced accuracy (BA). The BA is the average of the PAs. We used this metric as our classes are strongly imbalanced and thus the OA is not the best metric to characterize the classification results (Fernández et al., 2018).

3. Results

3.1. Rot detection

In Table 3 the best results obtained for each subset of ITCs are shown. If we consider all the ITCs the best result (BA = 56.1%) was obtained using all the indices extracted from all the images (13 images × 10 indices = 130 features). Looking at the PAs and UAs it is evident that there are some missed and false alarms in the prediction: regarding the missed alarms they are showed the PA and UA of the rot class that are quite low (48.4% and 32.7%), while the false alarms are highlighted by the not very high PA of the healthy class (64.3%). At the contrary, the best result (BA = 70.6%) considering only ITCs with area > 9 m² was obtained with the multi-temporal values of the GNDVI index extracted from the 2017 images, thus using just three input features. In this case there are still some missed and false alarms (PA and UA of the rot class of 66.4% and 55.6%) but they are reduced compared to the previous results.

It is worth noting that the proportion of samples between the classes "Healthy", "Rot" and "Other species" changes considering all ITCs and only ITCs with area > 9 m². In particular, in the first case the ITCs are distributed as 5689 "Healthy", 1654 "Rot" and 1146 "Other species"; while in the second case they are distributed as 214 "Healthy", 70 "Rot" and 384 "Other species". From these numbers it can be seen that the majority of the Norway spruce trees in the study area are smaller than 9

Table 3
Best results for rot classification obtained for each ITC area subsets. OA = overall accuracy; BA = balanced accuracy; PA = producer's accuracy; UA = user's accuracy.

ITC subset	Time periods	Feature	OA (%)	BA (%)	PA (%) Healthy	Rot	UA (%) Healthy	Rot
All	All	All	60.5	56.3	64.3	48.4	81.0	32.7
Area > 9 m^2	2017	GNDVI	72.5	70.6	74.8	66.4	91.3	55.6

m^2 as there is a huge decrease in the number of available ITCs between the two subsets. Simultaneously, the number of "Other species" ITCs increases (as proportion) as species different from Norway spruce in the study area (i.e. pines and broadleaves) tend to have larger crowns compared to Norway spruce.

In Fig. 4 the results in terms of balanced accuracy obtained for the rot detection with all combinations of features and time periods for all ITCs and only the ones with area > 9 m^2 are shown. The difference in accuracy is small between the time periods when all ITCs were subject to analysis, while the time period of year appeared to be a factor with great influence on the results when considering the ITCs with area > 9 m^2. In this case, the May, June and July images seem to outperform August and September. By averaging all the uni-temporal results against the multi-temporal results, the multi-temporal datasets resulted in greater

accuracy than the uni-temporal ones.

3.2. Tree species classification

In Table 4 the best results are shown for the detection of the tree species. As can be seen with all the ITCs, all the available features are used, and the results are good. As for the rot detection considering only ITCs with area > 9 m^2 the results are improving. Looking at Fig. 5 we can see that considering all ITCs and only the ones with area > 9 m^2, the results with an ITC area threshold of 9 m^2 are always superior to the others. There are five time periods for which results are showing high accuracies for both all ITCs and only the large ones (>9 m^2): i) all the time periods, ii) all the time periods in 2018, iii) all the time periods in 2019, iv) all the time periods for June, and v) all the time periods for
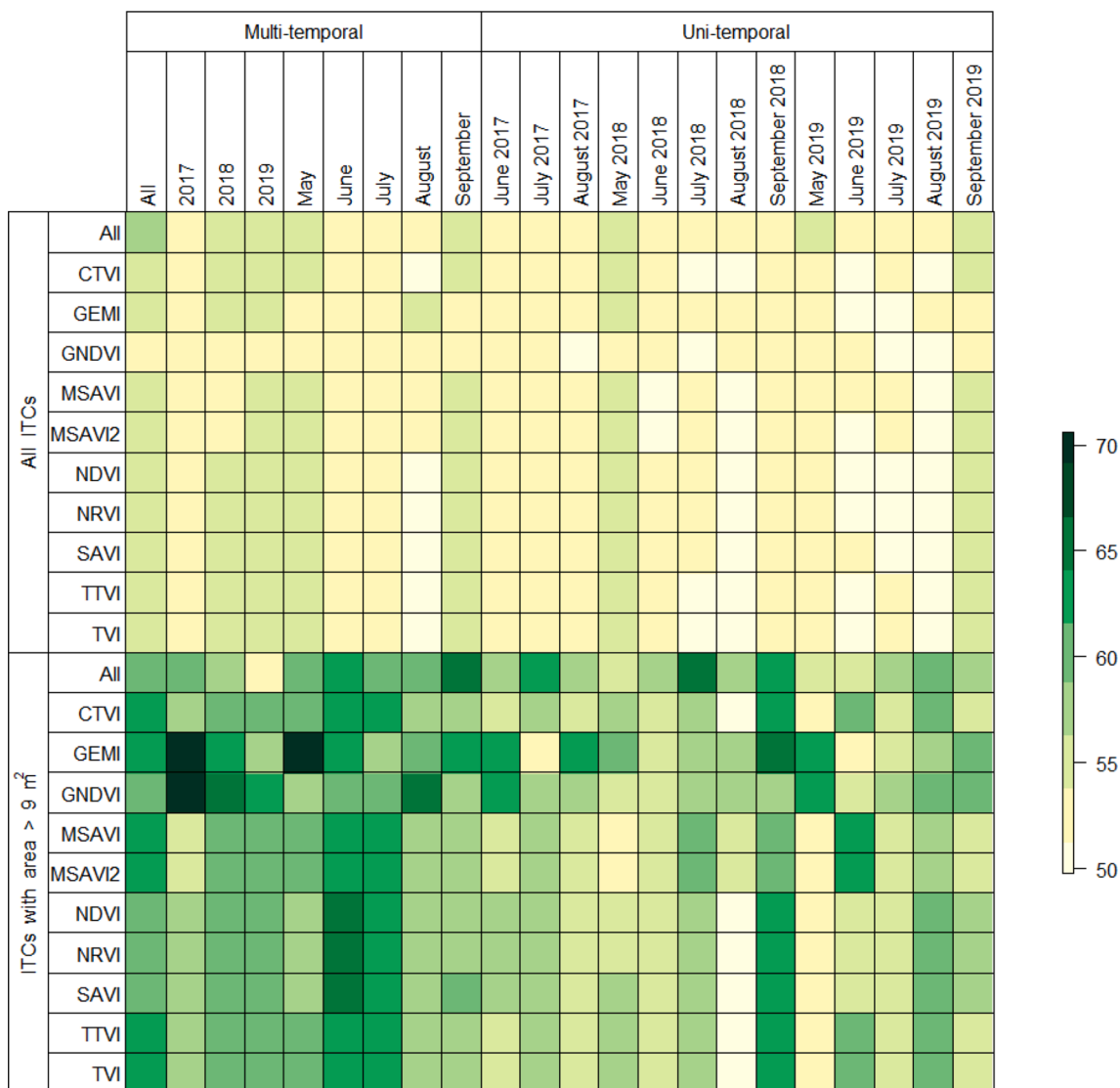

Fig. 4. Mean balanced accuracy for each experiment for rot detection. The names on the top describe the time period, while on the left there are the feature names and the ITC area thresholds.

Table 4
Best results for tree species classification obtained for each ITC area subsets. OA = overall accuracy; BA = balanced accuracy; PA = producer's accuracy; UA = user's accuracy.

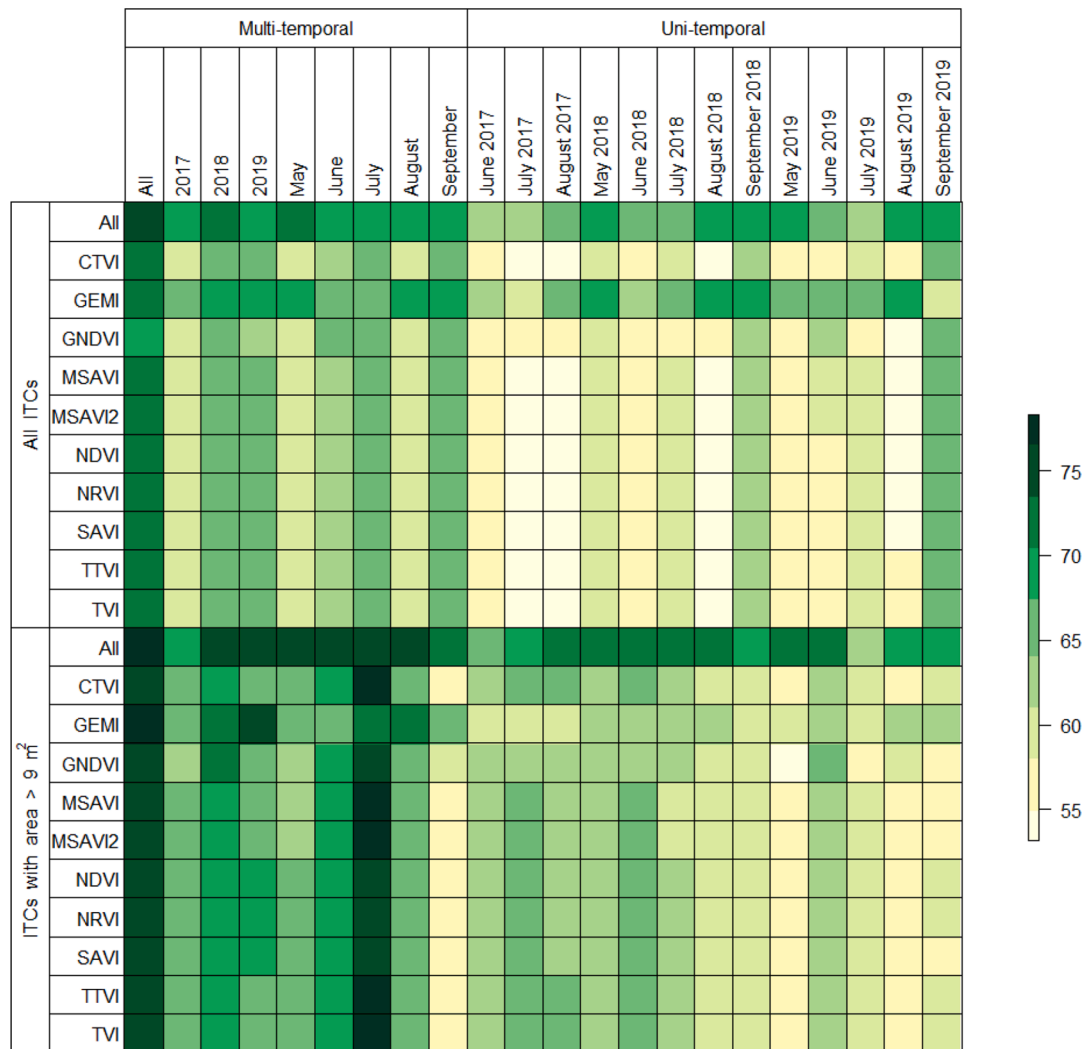| ITC subsets	Time periods	Feature	OA (%)	BA (%)	PA (%) Other species	Norway spruce	UA (%) Other species	Norway spruce
All	All	All	77	74.4	70.7	78.1	45.5	92.2
Area > 9 m²	All	GEMI	78.2	78.3	77.3	79.4	76.8	86.7

Fig. 5. Mean balanced accuracy for each experiment for tree species classification. The names on the top describe the considered time periods, while on the left there are the feature names and the ITC subsets.

July. Regarding the features, it seems that considering all the VIs or only the GEMI index were the best choices.

3.3. Rot map

In Fig. 6, the ITCs delineated using the lidar data covering the entire study area are shown by classification into three classes: healthy, rot and other species. The classification map at ITCs level (for both spruce and rot) was done using the models based on all ITCs. A confusion matrix (Table 5) and the corresponding accuracies were computed by matching the ITCs with the field dataset (as explained in the methods section). The BA of the map was 55.8% while the overall accuracy was 52.3%. Differently than before, these accuracies are on three classes and they are based on all the field data matched with an ITCs (8522 ITCs). By

looking at the map of Fig. 6, the ITCs affected by rot are clustered in some areas.

4. Discussion

Detecting rot in Norway spruce trees is without doubt of great relevance, since it could allow for decision makers to act and stop the propagation of the infection, hence reducing the economic losses that infected trees carry. Nevertheless, detecting rot is difficult because trees hardly show any visual signs of infection. In fact, rather few studies have been carried out in the literature with the aim of detecting rot in Norway spruce trees from remote sensing (Allen et al., 2022; Kankaanhuhta et al., 2000; Ostovar et al., 2019; Räty et al., 2021).

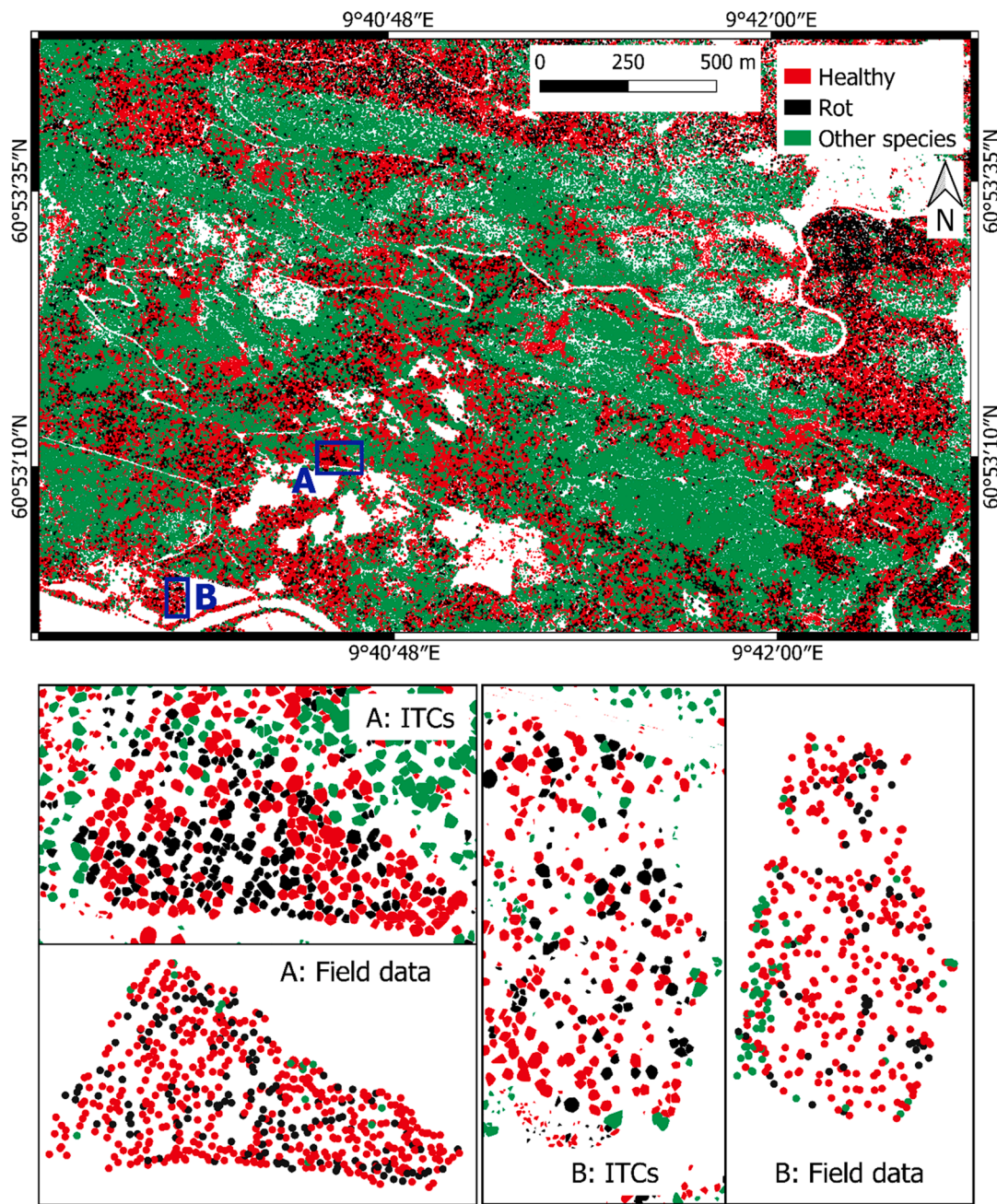In this study, we proposed an approach that went further on the rot

Fig. 6. Rot map over the study area, with zoom in over two areas of interest. The field data are represented by dots of the locations of the field trees.

Table 5
Confusion matrix for the species and rot map at ITC level (PA = producer's accuracy; UA = user's accuracy).

		Ground reference			
		Healthy	Rot	Other species	UA (%)
Classification	Healthy	2892	667	235	76.2
	Rot	1873	735	77	27.4
	Other species	952	263	828	40.5
	PA (%)	50.6	44.1	72.6	

infection detection process, by exploiting the multi-temporal variable. Firstly, we showed that combining Dove data with ITCs delineated by using lidar data, it is possible to construct close to tree level (given Dove's spatial resolution of 3 m that may contain more than a single tree) rot maps. To work at ITC level, it is necessary to have an

appropriate point density. With a very low point density it is not possible to delineate ITCs with a good level of accuracy and thus an ITC level analysis is not possible. Nowadays many lidar surveys are done with a point density around or above 10 pts/m^2 that is considered a good point density for ITCs detection. Kandare et al. (2016) showed that there was not a significant difference between 10 and 60 pts/m^2 in ITCs detection. There was an improvement increasing the density but not significant. ITCs can be obtained nowadays in many regions/countries for which data from regular lidar campaigns exist (e.g., programs with repeated acquisitions every 10 years or so). Since lidar information is essential for forest inventory, its availability will increase in more and more countries in the future. Nevertheless, approaching the problem in a different way, one could work at area-based level using satellite data at a coarser resolution compared to Dove. From a management point of view, the possibility of having a rot presence map at ITC level, allows punctual, as well as more precise, interventions in the forest. In this way the spread of

the fungi and therefore the economic loss could be minimized. The results from the present study could also help to develop better and more precise management strategies for forests, especially in commercially managed ones. Lastly, but most importantly, we showed how it is possible to achieve reasonable results regarding the rot detection by exploiting multi-temporal variables. Multi-temporal information allowed the identification of infected trees, leading to the construction of a reliable map (according to interpretation from experts in the topic and the studied area and according to the OA/BA) showing the possible locations of infected and healthy trees.

The balance accuracy values increased with the ITCs area, both for the tree species classification and for rot detection. This is reasonable and as one would expect because (i) the actual spatial resolution of the Dove images is of 9 m^2 and (ii) larger Norway spruce trees are expected to be the most mature ones. In the former case, this means that for trees having a crown that big, the degree of mixing with neighbouring trees and other land cover types is less present. Thus, a better representation of the spectral information and a better classification analysis can be carried out. In the latter case, it is known from the literature (Solheim, 2010; Stenlid and Wästerlund, 1986) that in older trees the rot spread is more pronounced.

An important factor that emerged from this study is that the use of multi-temporal information is providing generally better results compared to the use of uni-temporal information. As shown in Table 3 the best cases for all ITCs subset were multi-temporal combinations of VIs. Rot is a degenerative process that changes and evolves with time, and thus it is expected that comparing images acquired in different years could help detect changes. Moreover, there may also be seasonal changes that can be captured by the multi-temporal data, but they are only slightly visible in our data. Concerning the most important vegetation indexes, it seems that considering only large crowns GEMI and GNDVI are performing better, while with all the ITCs the results are better with all the indexes. In general all the considered indexes include the NIR band that could be influenced by changes in the crown density and structure due to the rot presence (Pitkänen et al., 2021; Žemaitis and Žemaitė, 2018).

As stated in the introduction, rot can be caused by many types of fungi. In this study, we did not differentiate between the different types of fungi as our field data, collected during the harvesting, was focused only on the presence of heartwood rot. It is worth noting that the same fungi that generated heartwood rot can also generate root rot that would not necessarily be visible on the cut stump at all. Thus, some trees that were considered as healthy in our dataset could in fact have been affected by root rot. This could be a factor contributing to false positives for the rot class. Moreover, each tree could have been subject to other types of stressors that were not detected during the field data collection and that also could have increased the number of false positives. Yet, the results show the potential of exploiting multi-temporal information to help in the rot detection.

To the best of our knowledge, only four other studies exist in literature that have carried out research to detect rot in Norway spruce trees with remote sensing (Allen et al., 2022; Kankaanhuhta et al., 2000; Ostovar et al., 2019; Räty et al., 2021). Three out of four of these studies did not work at ITC level. In particular, Kankaanhuhta et al. (2000) classified areas with predominance of healthy or infected trees, while Ostovar et al., (2019) classified stumps after the harvesting with high spatial resolution UAV data. Räty et al. (2021) did not focused directly on mapping rot presence but predicted rot volume at stand level combining both remote sensing (i.e., ALS and Sentinel-2 data) and environmental variables. The only study in the literature like the current one is the one of Allen et al. (2022) carried out on the same study area. In that study the authors used airborne hyperspectral data for a single date (30 cm spatial resolution) in order to classify only between rot and no-rot classes (the analysis is directly performed over Norway spruce trees). Comparing those results with the ones presented in Table 3 for all ITCs, the accuracies are comparable. The OA for Allen et al. (2022) is of 64.81%, compared to 60.5% for this paper. The UA's and PA's range from 59.61% to 70.04% for Allen et al. (2022) and from 48.4% to 81% for this paper. Taking into account that Dove's spatial resolution is 10 times lower than that of the aerial data used by Allen et al. (2022), we can conclude that the proposed approach could provide useful information for the heartwood rot detection in Norway spruce trees, by reducing the costs and time of those analysis.

Even though Norway spruce classification may be conducted in different ways, having a proper species classification map helps to better map the location of trees affected by rot in any studied area. Here, similar to the detection of rot trees, the balanced accuracy value remains relatively stable considering all tree areas and only the ITCs > 9 m^2 (see Table 4). For the multi-temporal case, all the VIs, together with multi-temporal data, helped to increase the balance accuracy. In the uni-temporal case, the best month for classification seemed to be July. The results obtained with ITCs with area > 9 m^2 are in line with what could be found in the literature. Dalponte et al (2013), for example, found similar accuracies using hyperspectral data (with spatial resolutions of 0.4 m and 1.5 m) and ranging from 68.5% − 79.2%, compared to 77% found in this paper for All ITCs areas with 3 m spatial resolution.

With the information on both rot and spruce location, a map showing infected trees (independently of the ITCs area) was constructed (see Fig. 6). This map and the corresponding confusion matrix (Table 5) demonstrated the usefulness of multi-temporal data, not only for properly mapping rot infection, but also for locating clusters of infected trees. As demonstrated in literature (Bovolo et al., 2018; Dalponte et al., 2020; Solano-Correa et al., 2020), multi-temporal's nature, of providing frequent observations of the same spot, makes it possible to clearly see different stages of a single (or different) phenomena happening in a given area. This nature is essential for studying phenomena, such as rot infection, that develop slowly over time, but leave traces that can be tracked when using the temporal variable, even if with low spatial resolution. Such information contributes to a continuous monitoring of the infected areas, as well as the development of damage containment plans, like planting other tree species in order to limit future damages and reduce the spread of the fungi.

Future developments could consider the study of other commercial satellites (e.g. WorldView constellation) that provide finer spatial resolution (finer than 1 m) with good temporal resolution (if data is available in archive or by ordering new acquisitions) or data fusion with hyperspectral data. Finer spatial and spectral resolutions could contribute to a better separability among the studied classes, leading to a higher UA and PA. Exploitation of further spectral information offered by future Dove satellites (up to 8 spectral bands instead of the current 4 ones) could be also considered in order to help for better separability among classes.

5. Conclusions

A method for the detection of rot in Norway spruce trees was proposed in this paper. The detection is performed at individual tree crown level. For this method, multi-temporal, multi-spectral images acquired by the Dove satellite constellation at 3 m spatial resolution, combined with different ITC areas, vegetation indices and time periods, were applied. Species classification was part of the method in order to improve rot detection/mapping. The results showed that detection models based on multi-temporal data performed better in classification of Norway spruce as well as classification of heartwood rot, when compared to results presented in literature and by considering low cost/ free satellite data. It was found that the best performance was achieved by considering multi-temporal information: (i) for 2017, with the GNDVI index and an ITC area > 9 m^2 (OA = 72.5%, BA = 70.6%), and (ii) all time periods in the case of All ITCs areas (OA = 60.5%, BA = 56.3%). This allowed not only to create a map showing both infected and healthy Norway spruce trees, but to map the location of other species not affected by rot (OA = 52.3%, BA = 56.3%). The obtained results provide useful information for detecting root rot and can help

forest managers to locate possible clusters of infected trees, and implement management strategies reducing the economic losses.

Declaration of Competing Interest

The authors declare that they have no known competing financial interests or personal relationships that could have appeared to influence the work reported in this paper.

Acknowledgements

References

Allen, B., Dalponte, M., Hietala, A., Ørka, H., Næsset, E., Gobakken, T., 2022. Detection of root, butt, and stem rot presence in Norway spruce with hyperspectral imagery. Silva Fenn 56 (2). https://doi.org/10.14214/sf.10606.

Axmon, J., Hansson, M., Sörnmo, L., 2004. Experimental study on the possibility of detecting internal decay in standing Picea abies by blind impact response analysis. For. Int. J. For. Res. 77, 179–192. https://doi.org/10.1093/forestry/77.3.179.

Bannari, A., Morin, D., Bonn, F., Huete, A.R., 1995. A review of vegetation indices. Remote Sens. Rev. 13 (1-2), 95–120. https://doi.org/10.1080/02757259509532298.

Baret, F., Guyot, G., 1991. Potentials and limits of vegetation indices for LAI and APAR assessment. Remote Sens. Environ. 35 (2-3), 161–173. https://doi.org/10.1016/0034-4257(91)90009-U.

Bovolo, F., Bruzzone, L., Solano-Correa, Y.T., 2018. Multitemporal Analysis of Remotely Sensed Image Data. In: Liang, S. (Ed.), Comprehensive Remote Sensing. Elsevier, Oxford, pp. 156–185. https://doi.org/10.1016/B978-0-12-409548-9.10338-0.

Chen, B., Shi, S., Gong, W., Zhang, Q., Yang, J., Du, L., Sun, J., Zhang, Z., Song, S., 2017. Multispectral LiDAR Point Cloud Classification: A Two-Step Approach. Remote Sens. 9, 373. https://doi.org/10.3390/rs9040373.

Coomes, D.A., Dalponte, M., Jucker, T., Asner, G.P., Banin, L.F., Burslem, D.F.R.P., Lewis, S.L., Nilus, R., Phillips, O.L., Phua, M.-H., Qie, L., 2017. Area-based vs tree-centric approaches to mapping forest carbon in Southeast Asian forests from airborne laser scanning data. Remote Sens. Environ. 194, 77–88. https://doi.org/10.1016/j.rse.2017.03.017.

Dalponte, M., Coomes, D.A., Murrell, D., 2016. Tree-centric mapping of forest carbon density from airborne laser scanning and hyperspectral data. Methods Ecol. Evol. 7 (10), 1236–1245. https://doi.org/10.1111/2041-210X.12575.

Dalponte, M., Frizzera, L., Gianelle, D., 2018. How to map forest structure from aircraft, one tree at a time. Ecol. Evol. 8 (11), 5611–5618. https://doi.org/10.1002/ece3.4089.

Dalponte, M., Marzini, S., Solano-Correa, Y.T., Tonon, G., Vescovo, L., Gianelle, D., 2020. Mapping forest windthrows using high spatial resolution multispectral satellite images. Int. J. Appl. Earth Obs. Geoinformation 93, 102206. https://doi.org/10.1016/j.jag.2020.102206.

Dalponte, M., Ørka, H.O., Ene, L.T., Gobakken, T., Næsset, E., 2014. Tree crown delineation and tree species classification in boreal forests using hyperspectral and ALS data. Remote Sens. Environ. 140, 306–317. https://doi.org/10.1016/j.rse.2013.09.006.

Dalponte, M., Orka, H.O., Gobakken, T., Gianelle, D., Naesset, E., 2013. Tree species classification in boreal forests with hyperspectral data. IEEE Trans. Geosci. Remote Sens. 51 (5), 2632–2645. https://doi.org/10.1109/TGRS.2012.2216272.

Dawn, S., Saxena, V., Sharma, B., 2010. Remote Sensing Image Registration Techniques: A Survey, in: Image and Signal Processing. Presented at the International Conference on Image and Signal Processing, Springer, Berlin, Heidelberg, pp. 103–112. https://doi.org/10.1007/978-3-642-13681-8_13.

Durbha, S.S., King, R.L., Younan, N.H., 2007. Support vector machines regression for retrieval of leaf area index from multiangle imaging spectroradiometer. Remote Sens. Environ., Multi-angle Imaging SpectroRadiometer (MISR) Special Issue 107 (1-2), 348–361. https://doi.org/10.1016/j.rse.2006.09.031.

Fensholt, R., Huber, S., Proud, S.R., Mbow, C., 2010. Detecting Canopy Water Status Using Shortwave Infrared Reflectance Data From Polar Orbiting and Geostationary Platforms. IEEE J Sel. Top. Appl. Earth Obs. Remote Sens. 3 (3), 271–285. https://doi.org/10.1109/JSTARS.2010.2048744.

Fernández, A., García, S., Galar, M., Prati, R.C., Krawczyk, B., Herrera, F., 2018. Learning from Imbalanced Data Sets. Springer International Publishing, Cham. https://doi.org/10.1007/978-3-319-98074-4.

Gavier-Pizarro, G.I., Kuemmerle, T., Hoyos, L.E., Stewart, S.I., Huebner, C.D., Keuler, N. S., Radeloff, V.C., 2012. Monitoring the invasion of an exotic tree (Ligustrum lucidum) from 1983 to 2006 with Landsat TM/ETM+ satellite data and Support Vector Machines in Córdoba, Argentina. Remote Sens. Environ., Landsat Legacy Special Issue 122, 134–145. https://doi.org/10.1016/j.rse.2011.09.023.

Gitelson, A.A., Merzlyak, M.N., 1998. Remote sensing of chlorophyll concentration in higher plant leaves. Adv. Space Res., Synergistic Use of Multisensor Data for Land Processes 22 (5), 689–692. https://doi.org/10.1016/S0273-1177(97)01133-2.

Huete, A.R., 1988. A soil-adjusted vegetation index (SAVI). Remote Sens. Environ. 25 (3), 295–309. https://doi.org/10.1016/0034-4257(88)90106-X.

Huse, K.J., Solheim, H., Venn, K., 1994. Stump inventory of root and butt rots in Norway spruce cut in 1992. Rapp. Fra Skogforskningen 23, 1–26.

Kandare, K., Ørka, H.O., Chan, J.-W., Dalponte, M., 2016. Effects of forest structure and airborne laser scanning point cloud density on 3D delineation of individual tree crowns. Eur. J. Remote Sens. 49 (1), 337–359. https://doi.org/10.5721/EuJRS20164919.

Kankaanhuhta, V., Mäkisara, K., Tomppo, E., Piri, T., Kaitera, J., 2000. Monitoring of diseases caused by Heterobasidion annosum and Peridermium pini in Norway spruce and Scots pine stands by airborne imaging spectrometry (AISA). In: Ukonmaanaho, L., Raitio, H. (Eds.), Forest Condition Monitoring in Finland - National Report 1999. Finnish Forest Research Institute.

Leckie, D.G., Jay, C., Gougeon, F.A., Sturrock, R.N., Paradine, D., 2004. Detection and assessment of trees with Phellinus weirii (laminated root rot) using high resolution multi-spectral imagery. Int. J. Remote Sens. 25 (4), 793–818. https://doi.org/10.1080/0143116031000139926.

Leutner, B., Horning, N., Schwalb-Willmann, J., Hijmans, R.J., 2019. RStoolbox: Tools for Remote Sensing Data Analysis.

Meddens, A.J.H., Hicke, J.A., Vierling, L.A., Hudak, A.T., 2013. Evaluating methods to detect bark beetle-caused tree mortality using single-date and multi-date Landsat imagery. Remote Sens. Environ. 132, 49–58. https://doi.org/10.1016/j.rse.2013.01.002.

Navarro-Cerrillo, R.M., Varo-Martínez, M.Á., Acosta, C., Palacios Rodriguez, G., Sánchez-Cuesta, R., Ruiz Gómez, F.J., 2019. Integration of WorldView-2 and airborne laser scanning data to classify defoliation levels in Quercus ilex L. Dehesas affected by root rot mortality: Management implications. For. Ecol. Manag. 451, 117564. https://doi.org/10.1016/j.foreco.2019.117564.

Nguyen, H.M., Demir, B., Dalponte, M., 2019. A weighted SVM-based approach to tree species classification at individual tree crown level using LiDAR data. Remote Sens. 11 (24), 2948. https://doi.org/10.3390/rs11242948.

Noordermeer, L., Sørngård, E., Astrup, R., Næsset, E., Gobakken, T., 2021. Coupling a differential global navigation satellite system to a cut-to-length harvester operating system enables precise positioning of harvested trees. Int. J. For. Eng. 32 (2), 119–127. https://doi.org/10.1080/14942119.2021.1899686.

Oliva, J., Julio Camarero, J., Stenlid, J., 2012. Understanding the role of sapwood loss and reaction zone formation on radial growth of Norway spruce (Picea abies) trees decayed by Heterobasidion annosum s.l. For. Ecol. Manag. 274, 201–209. https://doi.org/10.1016/j.foreco.2012.02.026.

Ostovar, A., Talbot, B., Puliti, S., Astrup, R., Ringdahl, O., 2019. Detection and classification of Root and Butt-Rot (RBR) in Stumps of Norway Spruce Using RGB Images and Machine Learning. Sensors 19, 1579. https://doi.org/10.3390/s19071579.

Peng, Y., Zhang, M., Xu, Z., Yang, T., Su, Y., Zhou, T., Wang, H., Wang, Y., Lin, Y., 2020. Estimation of leaf nutrition status in degraded vegetation based on field survey and hyperspectral data. Sci. Rep. 10, 4361. https://doi.org/10.1038/s41598-020-61294-7.

Pérez-Bueno, M.L., Pineda, M., Vida, C., Fernández-Ortuño, D., Torés, J.A., de Vicente, A., Cazorla, F.M., Barón, M., 2019. Detection of White Root Rot in Avocado Trees by Remote Sensing. Plant Dis. 103 (6), 1119–1125. https://doi.org/10.1094/PDIS-10-18-1778-RE.

Perry, C.R., Lautenschlager, L.F., 1984. Functional equivalence of spectral vegetation indices. Remote Sens. Environ. 14 (1-3), 169–182. https://doi.org/10.1016/0034-4257(84)90013-0.

Pinty, B., Verstraete, M.M., 1992. GEMI: a non-linear index to monitor global vegetation from satellites. Vegetatio 101 (1), 15–20. https://doi.org/10.1007/BF00031911.

Pitkänen, T.P., Piri, T., Lehtonen, A., Peltoniemi, M., 2021. Detecting structural changes induced by Heterobasidion root rot on Scots pines using terrestrial laser scanning. For. Ecol. Manag. 492, 119239. https://doi.org/10.1016/j.foreco.2021.119239.

PlanetTeam, 2017. Planet Application Program Interface: In Space for Life on Earth. San Fracisco, CA.

Qi, J., Chehbouni, A., Huete, A.R., Kerr, Y.H., Sorooshian, S., 1994. A modified soil adjusted vegetation index. Remote Sens. Environ. 48 (2), 119–126. https://doi.org/10.1016/0034-4257(94)90134-1.

Räty, J., Breidenbach, J., Hauglin, M., Astrup, R., 2021. Prediction of butt rot volume in Norway spruce forest stands using harvester, remotely sensed and environmental data. Int. J. Appl. Earth Obs. Geoinformation 105, 102624. https://doi.org/10.1016/j.jag.2021.102624.

Rouse, J.W, Haas, R.H., Schell, J.A., Deering, D.W., 1974. Monitoring vegetation systems in the Great Plains with ERTS. Proc. Third Earth Resour. Technol. Satell. 1 Symp.

Solano-Correa, Y.T., Bovolo, F., Bruzzone, L., 2019. Generation of Homogeneous VHR Time Series by Nonparametric Regression of Multisensor Bitemporal Images. IEEE Trans. Geosci. Remote Sens. 57 (10), 7579–7593. https://doi.org/10.1109/TGRS.2019.2914397.

Solano-Correa, Y.T., Bovolo, F., Bruzzone, L., Fernandez-Prieto, D., 2020. A Method for the Analysis of Small Crop Fields in Sentinel-2 Dense Time Series. IEEE Trans. Geosci. Remote Sens. 58 (3), 2150–2164. https://doi.org/10.1109/TGRS.2019.2953652.

Solheim, H., 2010. Råtesopper - i levende trær.

Song, X., Yang, C., Wu, M., Zhao, C., Yang, G., Hoffmann, W.C., Huang, W., 2017. Evaluation of Sentinel-2A Satellite Imagery for Mapping Cotton Root Rot. Remote Sens. 9, 906. https://doi.org/10.3390/rs9090906.

Sozzi, M., Marinello, F., Pezzuolo, A., Sartori, L., 2018. Benchmark of Satellites Image Services for Precision Agricultural use. Presented at the European Society of Agricultural Engineers 2018, Wageningen, the Netherlands. https://doi.org/10.3390/agronomy11112098.

Stenlid, J., Wästerlund, I., 1986. Estimating the frequency of stem rot in Picea abies using an increment borer. Scand. J. For. Res. 1 (1-4), 303–308. https://doi.org/10.1080/02827588609382421.

Su, H., Wu, X., Yan, X.-H., Kidwell, A., 2015. Estimation of subsurface temperature anomaly in the Indian Ocean during recent global surface warming hiatus from satellite measurements: A support vector machine approach. Remote Sens. Environ. 160, 63–71. https://doi.org/10.1016/j.rse.2015.01.001.

Thiam, A.K., 1998. Geographic information systems and remote sensing methods for assessing and monitoring land degradation in the Sahel region: The case of southern Mauritania. PhD Thesis.

Tondewad, M.P.S., Dale, M.M.P., 2020. Remote Sensing Image Registration Methodology: Review and Discussion. Procedia Computer Science 171, 2390–2399.

Versace, S., Gianelle, D., Frizzera, L., Tognetti, R., Garfì, V., Dalponte, M., 2019. Prediction of competition indices in a Norway spruce and silver fir-dominated forest using lidar data. Remote Sens. 11 https://doi.org/10.3390/rs11232734.

Vollbrecht, G., Agestam, E., 1995. Identifying butt rotted Norway spruce trees from external signs 1, 241–254.

Wermelinger, B., 2004. Ecology and management of the spruce bark beetle Ips typographus—a review of recent research. For. Ecol. Manag. 202 (1-3), 67–82. https://doi.org/10.1016/j.foreco.2004.07.018.

Wu, M., Yang, C., Song, X., Hoffmann, W.C., Huang, W., Niu, Z., Wang, C., Li, W., Yu, B., 2018. Monitoring cotton root rot by synthetic Sentinel-2 NDVI time series using improved spatial and temporal data fusion. Sci. Rep. 8, 2016. https://doi.org/10.1038/s41598-018-20156-z.

Žemaitis, P., Žemaitė, I., 2018. Does butt rot affect the crown condition of Norway spruce trees? Trees 32 (2), 489–495. https://doi.org/10.1007/s00468-017-1645-0.

Zhao, K., Suarez, J.C., Garcia, M., Hu, T., Wang, C., Londo, A., 2018. Utility of multitemporal lidar for forest and carbon monitoring: Tree growth, biomass dynamics, and carbon flux. Remote Sens. Environ. 204, 883–897. https://doi.org/10.1016/j.rse.2017.09.007.